

Dynamics of an acoustically trapped sphere in beating sound waves

Mohammed A. Abdelaziz and David G. Grier

Department of Physics and Center for Soft Matter Research, New York University, New York, NY 10003

(Dated: September 1, 2020)

A focused acoustic standing wave creates a Hookean potential well for a small sphere and can levitate it stably against gravity. Exposing the trapped sphere to a second transverse travelling sound wave imposes an additional acoustical force that drives the sphere away from its mechanical equilibrium. The driving force is shaped by interference between the standing trapping wave and the traveling driving. If, furthermore, the traveling wave is detuned from the standing wave, the driving force oscillates at the difference frequency. Far from behaving like a textbook driven harmonic oscillator, however, the wave-driven harmonic oscillator instead exhibits a remarkably rich variety of dynamical behaviors arising from the spatial dependence of the driving force. These include oscillations at both harmonics and subharmonics of the driving frequency, period-doubling routes to chaos and Fibonacci cascades. This model system therefore illustrates opportunities for dynamic acoustical manipulation based on spectral control of the sound field, rather than spatial control.

Acoustical manipulation is emerging as an attractive alternative to optical manipulation for applications where large forces are required to move sizeable objects over macroscopic distances [1–5]. Sound waves can exert far more force per watt than light waves [6, 7], but are not yet so easy to control. Optical techniques have the advantage in this regard thanks to a wealth of technology for controlling the spatial structure of laser beams. Dynamic holographic optical trapping, for example, uses megapixel arrays of phase-shifting elements to sculpt an ordinary laser beam into complex three-dimensional optical force fields [8, 9]. Analogous devices for sound are under development [2, 10–12], but do not yet offer the same degree of control afforded by their optical counterparts.

One respect in which sound has a clear advantage over light is the ease with which a coherent sound wave’s frequency can be altered. The present study illustrates the opportunities for dexterous and dynamic acoustical manipulation afforded by spectral engineering through experimental and numerical studies of a deceptively simple dynamical system assembled and actuated by two continuous sound waves. Slightly detuning the two waves gives rise to a remarkably rich and potentially useful spatiotemporal phenomenology without requiring active control of the force field’s structure.

Our system, shown schematically in Fig. 1(a), consists of a small sphere of mass m that is stably levitated in air by a vertical standing-wave acoustical trap at frequency ω . The standing wave’s transverse intensity gradients give rise to a restoring force that localizes the sphere in a three-dimensional harmonic well with natural frequency $\omega_0 \ll \omega$. The trapped sphere also is exposed to a travelling sound wave at frequency $\omega + \Delta\omega$ that is projected horizontally. Interference between the two sound waves creates a force field for the sphere that oscillates at the difference frequency, $\Delta\omega$. Unlike conventional harmonic driving, however, this force field also depends on position because the interference pattern that drives the sphere takes the form of a traveling wave. The driving force experienced by the sphere therefore depends on its position within its trap. The state dependence

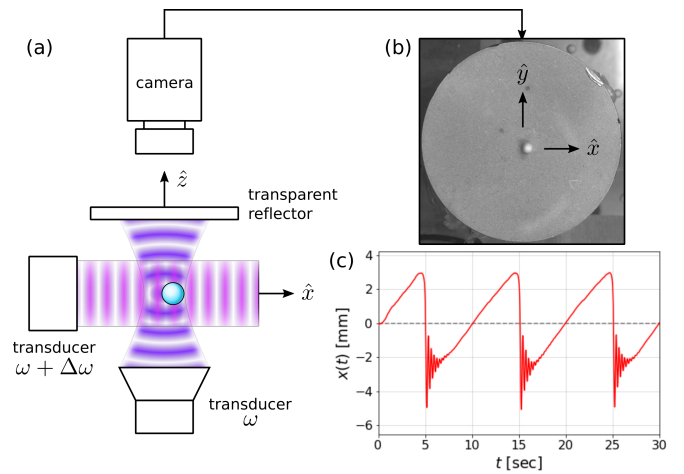


FIG. 1. (a) Schematic representation of an acoustically levitated particle driven by a harmonic traveling wave. (b) Video frame showing a top view of the particle at $z = 4$ mm above the transducer in a standing wave at $f = 40.3$ kHz. (c) Measured trajectory, $x(t)$, of the particle driven by a difference frequency, $\Delta f = 0.1$ Hz.

of wave-mediated driving gives rise to a remarkably rich phenomenology that includes period-doubling paths to chaos and Fibonacci cascades in addition to robust scanning modes that hold the promise of practical applications [11, 12].

The vertical acoustical trap in our instrument is created by a 40 kHz piezoelectric transducer (Sunnytec Electronics, STC-4SH-3540(B)) that is driven near resonance by a function generator (Stanford Research Systems DS345). The transducer has a conical aluminum horn with a 4.5 cm-diameter output coupler that slightly concentrates the sound wave on the acoustical axis. This wave is reflected by a horizontal plexiglas sheet to form a standing-wave acoustical trap. The plexiglas reflector is positioned around 6 cm above the transducer using a micrometer drive (Prior FB201 Manual Focus Block). Its height is adjusted to maximize the amplitude of the

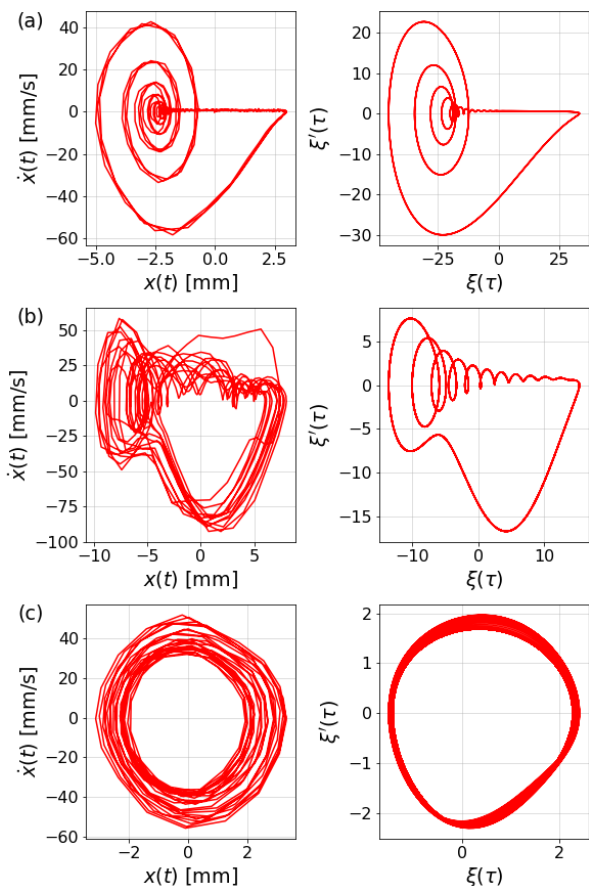


FIG. 2. Comparison between experimentally measured trajectories, $x(t)$, in the left column and numerical solutions to Eq. (2), $\xi(\tau)$, in the right column. Data are plotted as phase space trajectories, $\dot{x}(x)$ and $\xi'(\xi)$, respectively. (a) $\Delta f = 0.1$ Hz; data replotted from Fig. 1(c). $\Omega = 1/20$, $\epsilon = 33$. (b) $\Delta f = 1.0$ Hz; $\Omega = 1/3$, $\epsilon = 15$. (c) $\Delta f = 2.5$ Hz; $\Omega = 1$, $\epsilon = 1$. All calculations assume $b = 0.3$.

pressure wave at the reflector's surface, as measured by a piezoelectric transducer and a lock-in amplifier (Stanford Research Systems, SR830) referenced to the function generator.

The transverse traveling wave is created by a smaller 40 kHz piezoelectric transducer (American Piezo, 10-3155) driven by a second function generator (Feeltech, FY6600) whose time base is tied to the first to ensure relative phase stability. The frequency and amplitude of this wave are adjusted to control the dynamical state of the levitated bead.

The transparent reflector also provides optical access, allowing us to record the sphere's motions in the horizontal plane at 40 frames/s with a magnification of 0.1 mm/pixel by a vertically oriented video camera (FLiR, Flea 3 monochrome). Figure 1(b) presents one video frame showing a 2 mm-diameter styrofoam bead stably levitated roughly 1 mm above the transducer's surface by a standing wave at $f = \omega/(2\pi) = 40.3$ kHz.

The trace in Fig. 1(c) shows the bead's measured tra-

jectory along \hat{x} when the driving wave is detuned from the trapping wave by $\Delta f = \Delta\omega/(2\pi) = 0.1$ Hz. The bead's position in each video frame is monitored with 10 μm precision using the `trackpy` particle-tracking library [13, 14]. This trace embodies both the promise and the challenge of the spectral control afforded by acoustical forces. Rather than undergoing simple harmonic motion, the floating bead sweeps out a nearly linear sawtooth pattern with distinct ringing on the flyback. This mode of motion resembles the linear scanners that have been demonstrated with acoustical and optical holographic trapping [11, 15, 16]. Whereas holographic control requires hundreds or millions of dynamically controlled monochromatic wave sources, spectral control achieves equivalent motion along a single axis using just two steady-state waves.

Sawtooth oscillation is just one of many modes of motion for the wave-driven acoustical oscillator. The range of possibilities is illustrated by an idealized model for the dynamics of an object in the acoustical force field. Working in Cartesian coordinates with \hat{z} aligned vertically and \hat{x} directed along the travelling wave, the sphere's horizontal displacement from its equilibrium position may be modelled as

$$\frac{d^2x}{dt^2} + \gamma \frac{dx}{dt} + \omega_0^2 x = \frac{F_0}{m} e^{i(kx - \Delta\omega t)}, \quad (1)$$

where γ is the damping rate, k is the wavenumber of the traveling wave, and F_0 is the scale of the transverse driving force. This model for the driving force is derived from the theory of acoustical forces in Appendix A. To explore the phenomenology of the wave-driven oscillator, we recast Eq. (1) in terms of the dimensionless displacement, $\xi(\tau) = kx$, and the dimensionless time, $\tau = \omega_0 t$, to obtain the non-dimensional equation of motion

$$\xi'' + b\xi' + \xi = \epsilon \exp(i\xi - i\Omega\tau), \quad (2)$$

where $b = \gamma/\omega_0$, $\Omega = \Delta\omega/\omega_0$, $\epsilon = kF_0/(m\omega_0^2)$, and primes denote derivatives with respect to τ .

Despite its close resemblance to the canonical model for a periodically driven harmonic oscillator, Eq. (2) does not have analytic solutions. We therefore solve Eq. (2) numerically using the LSODA integrator with 128 steps per driving period, running the integration for 2048 periods to permit transients to decay before recording trajectory data for analysis.

Figure 2 provides a sense of the variety of operating states of the experimental oscillator and the ability of Eq. (2) to capture its behavior. The left column shows experimentally measured phase-space trajectories, $\dot{x}(x)$, for three different values of the detuning: (a) $\Delta f = 0.1$ Hz, which also appears in Fig. 1(c); (b) $\Delta f = 1$ Hz; and (c) $\Delta f = 2.5$ Hz. The right column shows corresponding phase-space trajectories, $\xi'(\xi)$, that are computed with Eq. (2). These are not fits to the experimental data, but rather are comparisons at roughly equivalent ratios of driving frequencies, with fixed damping rate, $b = 0.3$,

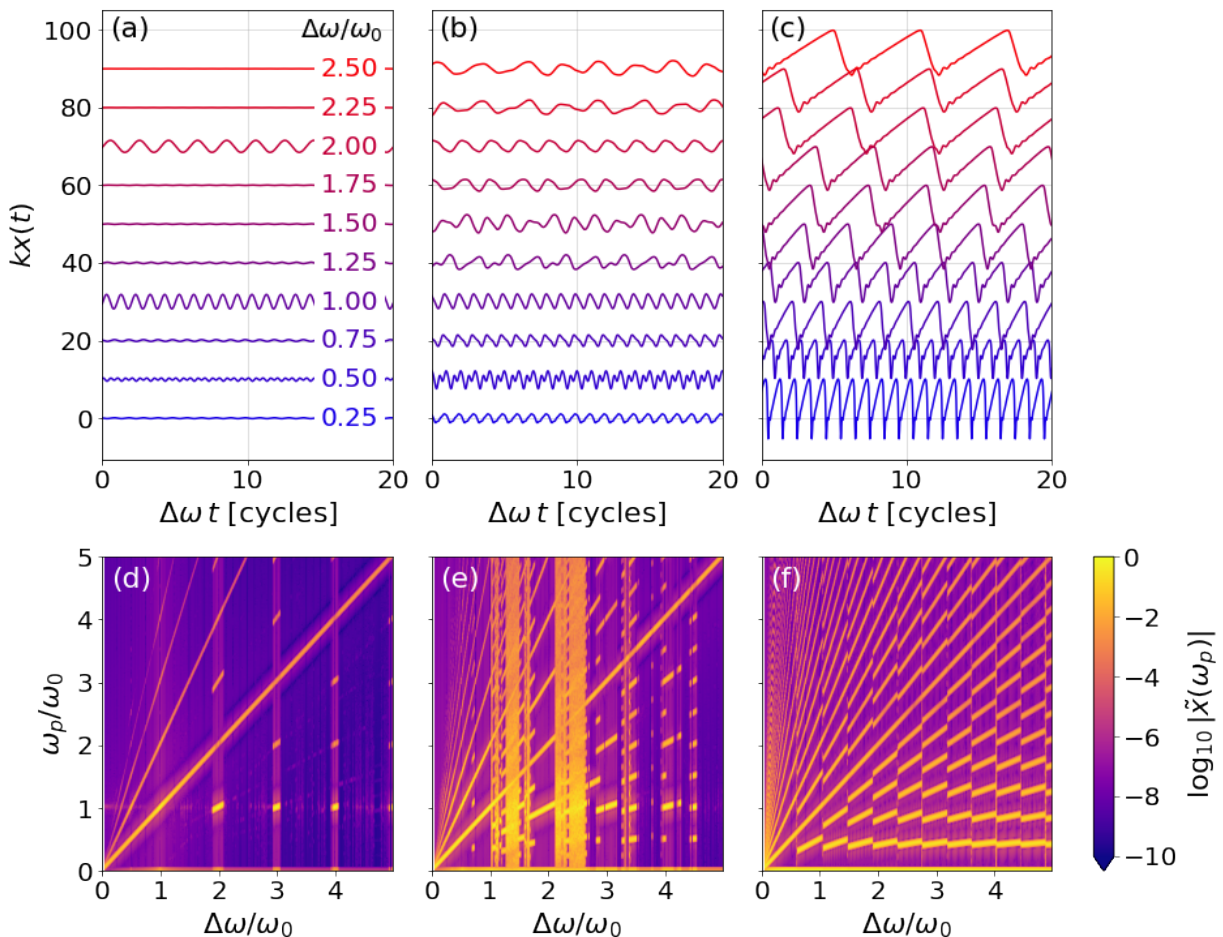


FIG. 3. Computed trajectories for (a) weak driving ($\epsilon = 0.1$, $b = 0.01$), (b) critical driving ($\epsilon = 1$, $b = 0.1$), and (c) strong driving ($\epsilon = 10$, $b = 1$) for driving frequencies ranging from $\Delta\omega = 0.25\omega_0$ to $\Delta\omega = 2.5\omega_0$. Curves are offset in steps of 10 for clarity and are colored by values of $\Delta\omega/\omega_0$. The corresponding power spectra, $|\tilde{x}(\omega_p)|$, in (d), (e) and (f) reveal markedly different behavior in the different dynamical regimes. These spectrograms are computed at frequency intervals of $0.05\omega_0$ and cover the range from $\Delta\omega = 0.1\omega_0$ to $5\omega_0$. Each is normalized to its maximum value.

and with driving amplitude adjusted to yield good qualitative agreement. Differences between the experimental and numerical solutions may be ascribed to nonideal properties of the physical system, but also reflect the immense richness of the system's full phenomenology.

Figure 3 presents numerical solutions to Eq. (2) in three dynamical regimes: (a) weak driving, $\epsilon \ll 1$, in which the particle undergoes nearly harmonic oscillations; (b) critical driving, $\epsilon = 1$, in which harmonic oscillation gives way to chaos; and (c) strong driving, $\epsilon \gg 1$, which is characterized predominantly by sawtooth oscillations. All three modes of operation are evident in the experimentally observed behavior of a levitated sphere.

Figure 3 also presents power spectra,

$$|\tilde{x}(\omega_p)| = \left| \int_{-\infty}^{\infty} W(t) x(t) e^{i\omega_p t} dt \right|, \quad (3)$$

computed from the sphere's trajectory for each of the three sets of driving amplitudes and for driving frequencies ranging from $\Delta\omega = 0.1\omega_0$ to $\Delta\omega = 5\omega_0$. In each

case, the dimensionless damping rate is set to $b = \epsilon/10$. Power spectra are computed from 128 driving cycles obtained after transients have decayed. Numerical artifacts due to the finite signal duration are suppressed with a normalized Blackman-Harris window function, $W(t)$. Driving and response frequencies in Figs. 3(d), (e) and (f) are scaled by the oscillator's natural frequency, ω_0 , which reflects the kinematics of the sphere in the optical trap, rather than an inherent property of the sound.

The continuous unit-slope diagonal peaks in all three spectrograms represent the oscillator's response at the driving frequency, which is the expected behavior for a driven harmonic oscillator. Features above the diagonal represent harmonics of the driving. Those below represent subharmonics.

The weakly driven oscillator in Fig. 3(d) displays a spectrum that is composed of (continuous) harmonics of the driving frequency superposed with (discrete) harmonics of the natural frequency, the latter appearing when the driving frequency is an integer multiple of the natu-

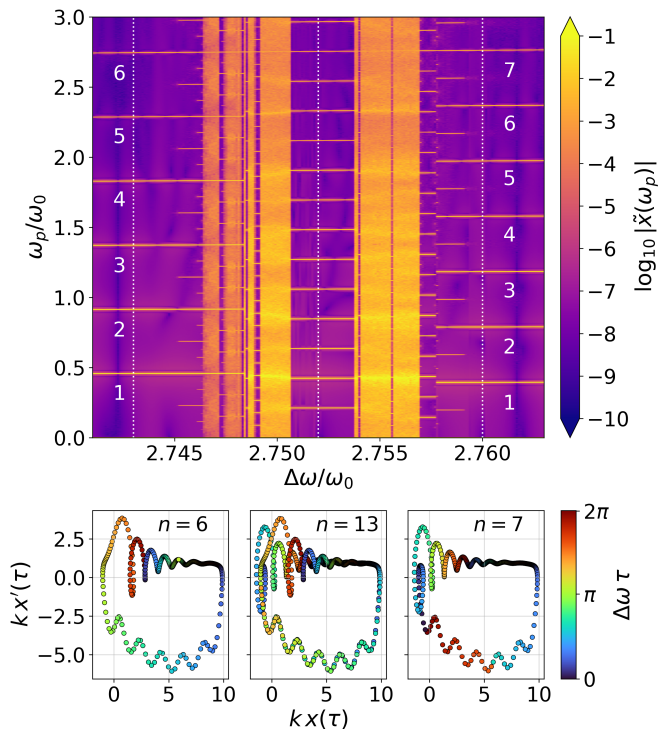


FIG. 4. Detailed view of the transition from the $n = 6$ subharmonic state to the $n = 7$ state, showing a period-doubling path to chaos and a Fibonacci cascade. Phase-space plots show one cycle of $n = 6$ and $n = 7$ states bounding the Fibonacci $n = 13$ state which appears as a strictly alternating sequence of $n = 6$ and $n = 7$ trajectories. Trajectory points are colored by periods of the driving frequency as indicated in the color bar. Vertical dotted lines on the spectrogram indicate driving frequencies for the phase-space trajectories.

ral frequency. These qualitative features are captured by a perturbative treatment of Eq (2) in Appendix B.

The spectrum becomes far more complex at critical driving in Fig. 3(e), with harmonics of the natural frequency being joined by subharmonics of the natural frequency and domains of broadband noise.

The remarkable spectrogram in Fig. 3(f) suggests that strong driving supports a sequence of abrupt transitions between dynamical states characterized by subharmonics of the driving frequency. Each state is composed of sawtooth waves whose appearance under strong driving conditions is motivated by a simplified model in Appendix C. Whereas such subharmonics are tied to resonance-like harmonics of the fundamental frequency under weak driving conditions in Fig. 3(d), they appear as continuous bands centered around period-2 subharmonics of the fundamental under strong driving conditions. The transitions between these dynamical states are not simply aligned with multiples of the fundamental frequency, nor, indeed, are they simply step-like.

Figure 4 presents a higher resolution map of the transition between period-6 and period-7 states that appears as a simple step near $\Omega = 2.75$ in Fig. 3(f). The contin-

uous peak near the top of this plot corresponds to the fundamental response, $\omega_p = \Delta\omega$. Numbered peaks identify subharmonics with the family of $n = 6$ subharmonics on the low-frequency side and $n = 7$ subharmonics on the high-frequency side.

Following the states up from low frequency reveals that the $n = 6$ state transitions to $n = 12$ and $n = 24$, following a period-doubling route to a chaotic state characterized by a broad-band power spectrum. Intriguingly, the period-doubling cascade from $n = 7$ toward lower frequencies appears to be cut off by the incommensurability between $n = 6$ and $n = 7$ states.

The phase-space plots in Fig. 4 show that the $n = 7$ state principally differs from the $n = 6$ state by the appearance of an additional loop in the phase-space trajectory. Vertical (white) dotted lines indicate the frequencies at which these trajectories were computed. Rather than appearing continuously the additional loop is introduced through a cascade of intermediate states. The intermediate $n = 13$ state, for example, is composed of a strict alternation between $n = 6$ and $n = 7$ states. The sampled frequency also is indicated in Fig. 4. We therefore recognize $n = 13$ as a Fibonacci state composed of the sum of the two states to either side in the frequency representation. Higher-order Fibonacci states also appear in the transition from $n = 6$ to $n = 7$, involving more complicated sequences of $n = 6$ and $n = 7$. Similar combinations of period-doubling cascades to chaos and Fibonacci cascades appear at the transitions between each of the principal subharmonic states in Fig. 3. Comparable intermediate states appear at each of the steps in Fig. 3(f).

This study introduces a one-dimensional acoustical scanner created from two waves. Adding an orthogonal driving transducer at a third frequency creates opportunities for two-dimensional scanning. More generally, three detuned traveling waves should create a dynamic volumetric force field that can translate one or more object through three-dimensional trajectories that are programmed by the differences in the waves' frequencies. Dynamic control over those frequencies promises still more dextrous control in three dimensions while using fewer transducers than a holographic array. Faster motion in this case is achieved with larger detuning, which is technically simpler than rapid reconfiguration of acoustic holograms.

Realizing the potential of spectral control for practical large-scale manipulation requires a deeper understanding of the dynamics of wave-driven harmonic oscillators. Analytic solutions to Eq. (2), for the minimal example presented in this study, for example, would guide development of practical acoustomechanical scanners. Detuned coaxial acoustical Bessel beams, for example, should act as high-speed tractor beams for transporting material [17] through their analogy to optical conveyors [18, 19]. Spectral control of acoustical force landscapes [20] also will create new opportunities for influencing the organization of multi-particle systems [21] by introducing a new

mechanism for controlling inter-particle interactions.

This work was supported by the MRSEC program of the National Science Foundation under Award Number DMR-1420073.

Appendix A: Acoustical forces in the wave-driven oscillator

The time-averaged acoustic radiation force on a small sphere of radius a_p at position \mathbf{r} in a harmonic pressure field $p(\mathbf{r}, t)$ is well-approximated by the Gor'kov potential [22, 23]:

$$U(\mathbf{r}) = \pi a_p^3 \rho_m \left[f_0 \frac{\langle |p(\mathbf{r}, t)|^2 \rangle}{3\rho_m^2 c_m^2} - f_1 \frac{\langle |\mathbf{v}(\mathbf{r}, t)|^2 \rangle}{2} \right], \quad (\text{A1})$$

where the coupling due to compressibility and density mismatches between the particle and medium are respectively described by

$$f_0 = 1 - \frac{\rho_m c_m^2}{\rho_p c_p^2} \quad \text{and} \quad (\text{A2a})$$

$$f_1 = \frac{2(\rho_p - \rho_m)}{2\rho_p + \rho_m}. \quad (\text{A2b})$$

The symbols ρ and c denote density and sound speed, respectively. Subscripts p and m refer to the particle and medium, respectively. In the system under study, the acoustic contrast between the sphere and air is large enough that $f_0 \approx f_1 \approx 1$. Angle brackets in Eq. (A1) signify time averages.

The velocity field is related to the pressure field in linear sound by Newton's second law,

$$\rho_m \frac{\partial \mathbf{v}}{\partial t} + \nabla p = 0. \quad (\text{A3})$$

For a harmonic wave at frequency ω , therefore, the pressure acts as a scalar potential for the velocity,

$$\mathbf{v}(\mathbf{r}, t) = -\frac{i}{\omega \rho} \nabla p. \quad (\text{A4})$$

Equations (A1) and (A4) define the acoustic force field established by a specified pressure field, $p(\mathbf{r}, t)$.

The wave-driven oscillator is subject to two harmonic pressure fields: a standing wave,

$$p_1(\mathbf{r}, t) = u_1 \sin(k_1 z) e^{-i\omega_1 t} \quad (\text{A5a})$$

at frequency ω_1 that forms an acoustical trap and a traveling wave,

$$p_2(\mathbf{r}, t) = u_2 e^{ik_2 x} e^{-i\omega_2 t}, \quad (\text{A5b})$$

at frequency ω_2 that provides the driving. To ensure that the amplitudes u_1 and u_2 are real-valued we absorb

spatial and temporal phase differences into the definitions of x and t .

The total pressure field, $p(\mathbf{r}, t) = p_1(\mathbf{r}, t) + p_2(\mathbf{r}, t)$, has an intensity

$$|p(\mathbf{r}, t)|^2 = |p_1|^2 + |p_2|^2 + 2\Re\{p_1^* p_2\} \quad (\text{A6})$$

that includes time-independent single-field intensities

$$|p_1|^2 + |p_2|^2 = u_1^2 \sin^2(k_1 z) + u_2^2 \quad (\text{A7})$$

and a time-dependent cross term,

$$2\Re\{p_1^* p_2\} = 2u_1 u_2 \text{sinc}(\phi) \times \sin(k_1 z) \cos(k_2 x - \Delta\omega t - \phi), \quad (\text{A8})$$

that oscillates at the difference frequency, $\Delta\omega = \omega_2 - \omega_1$. The phase offset, $\phi = \pi\Delta\omega/\omega$, depends on the detuning of the two waves relative to the center frequency $\omega = (\omega_1 + \omega_2)/2$ and contributes to the amplitude of the cross term. Pursuing a similar line of reasoning for the velocity yields

$$|\mathbf{v}(\mathbf{r}, t)|^2 = |\mathbf{v}_1|^2 + |\mathbf{v}_2|^2 + 2\Re\{\mathbf{v}_1^* \cdot \mathbf{v}_2\} \quad (\text{A9})$$

$$= \frac{u_1^2}{\rho_m^2 c_m^2} \cos^2(k_1 z) + \frac{u_2^2}{\rho_m^2 c_m^2}, \quad (\text{A10})$$

with the cross term vanishing because the two waves are orthogonal. Dropping constant terms, we obtain a time-dependent potential,

$$U(\mathbf{r}, t) = A \cos^2(k_1 z) + B \sin(k_1 z) \cos(k_2 x - \Delta\omega t), \quad (\text{A11})$$

that includes an axial trapping potential whose scale is set by the standing wave,

$$A = \frac{1}{6} u_1^2 \frac{\pi a_p^3}{\rho_m c_m^2}, \quad (\text{A12})$$

and a time-dependent contribution that arises from the interference between the standing and traveling wave,

$$B = \frac{2}{3} u_1 u_2 \frac{\pi a_p^3}{\rho_m c_m^2}. \quad (\text{A13})$$

In the absence of external forces, the trapping potential due to the standing wave would tend to localize the particle near $k_1 z = \pi/2$, which would effectively suppress the transverse driving force. Gravity, however, displaces the particle downward to

$$z_0 \approx -\frac{1}{2k_1} \sin\left(8 \frac{\rho_p \rho_m c_m^2 g}{u_1^2}\right), \quad (\text{A14})$$

where g is the acceleration due to gravity. The resulting transverse force then becomes

$$F(\mathbf{r}, t) = F_0 \sin(k_2 x - \Delta\omega t), \quad (\text{A15})$$

with the force scale $F_0 = -k_2 B \sin(k_1 z_0)$. This motivates the choice of a wavelike driving force for the right-hand side of Eq. (1) in the main text.

In the interest of clarity, this analysis has not accounted for the transverse trapping force arising from transverse gradients in the vertical standing wave, but rather has treated the standing wave as plane-like near the trapping plane. A more complete treatment yields an expression comparable to Eq. (A15) with corrections to the scale factor, F_0 . Interestingly, wave-like driving in this system appears to rely on gravity to displace the trapped particle. We predict therefore that the effects observed in this study would not occur under density-matched conditions or in microgravity.

Appendix B: Weak driving in the underdamped regime

The wave-driven oscillator does not behave like a standard periodically-driven harmonic oscillator even when weakly driven, as illustrated by Fig. 3(d) in the main text. We explain qualitative features of this system's dynamics by treating Eq. (2) from the main text perturbatively in the limit of weak driving ($\epsilon < 1$) when damping may be ignored ($b \ll 1$):

$$\xi''(\tau) + \xi(\tau) \approx \epsilon e^{i\xi(\tau) - i\Omega\tau}. \quad (\text{A1})$$

Substituting a trial solution

$$\xi(\tau) = \xi_0(\tau) + \epsilon\xi_1(\tau) + \epsilon^2\xi_2(\tau) + \dots, \quad (\text{A2})$$

with initial conditions $\xi_n(0) = \xi'_n(0) = 0$ yields for the first few terms

$$\xi_0(\tau) = 0 \quad (\text{A3a})$$

$$\xi_1(\tau) = \frac{e^{-i\Omega\tau}}{1 - \Omega^2} + \frac{1}{2} \left(\frac{e^{-i\tau}}{\Omega - 1} - \frac{e^{i\tau}}{\Omega + 1} \right) \quad (\text{A3b})$$

$$\begin{aligned} \xi_2(\tau) = & i \frac{e^{-2i\Omega\tau}}{(\Omega^2 - 1)(4\Omega^2 - 1)} \\ & - \frac{i}{2\Omega} \left[\frac{e^{-i\tau}}{(\Omega - 2)(2\Omega - 1)} - \frac{e^{i\tau}}{(\Omega + 2)(2\Omega + 1)} \right] \\ & - \frac{i}{2\Omega} \left[\frac{e^{-i(\Omega+1)\tau}}{(\Omega - 1)(\Omega + 2)} - \frac{e^{-i(\Omega-1)\tau}}{(\Omega + 1)(\Omega - 2)} \right]. \end{aligned} \quad (\text{A3c})$$

The first-order contribution in Eq. (A3b) includes a response at the the driving frequency, Ω , that is expected for a driven harmonic oscillator. It also includes a response at the natural frequency, $\omega_p = \omega_0$, that appears

regardless of the driving frequency, and is resonantly enhanced when $\Omega = \pm 1$. This appears in Fig. 3(d) as a horizontal streak at $\omega_p = \omega_0$.

The second-order contribution from Eq. (A3c) includes the second harmonic of the driving frequency, which appears in Fig. 3(d) as a continuous diagonal streak at $\omega_p = 2\Delta\omega$. The second term in Eq. (A3c) contributes to the oscillator's response at the natural frequency, with additional resonant enhancement at $\Omega = \pm 2$ and $\Omega = \pm 1/2$. The third term describes sum- and difference-frequency responses at $\omega_p = \Delta\omega \pm \omega_0$ that are resonantly enhanced near $\Omega = 2$. This contribution accounts for the frequency dependence of the observed peaks in Fig. 3(d) near $\omega_p = \omega_0$ and $\omega_p = 3\omega_0$ for driving frequencies in the vicinity of $\Delta\omega = 2\omega_0$.

Higher-order terms introduce corresponding harmonics of the driving frequency as well as the sum- and difference-frequency responses that account for the grid of discrete resonant peaks in Fig. 3(d).

Appendix C: Strong driving in the overdamped regime

The sawtooth oscillations observed in Fig. 3(c) from the main text under strong driving conditions, $\epsilon > 1$, feature long stretches of nearly linear motion punctuated by abrupt changes in direction. The equation of motion from Eq. (2) in the main text may be approximated in these weakly inertial passages by the transcendental equation

$$\xi = \epsilon \sin(\xi - \Omega\tau). \quad (\text{A1})$$

For large ϵ , the object follows the wave until $\xi \approx \epsilon$, at which point the restoring force overcomes the driving force and the object snaps back. This occurs at $\tau = \epsilon/\Omega$ which suggests the the fundamental oscillation frequency,

$$\omega_p = 2\pi\Delta\omega \frac{m\omega_0^2}{kF_0}, \quad (\text{A2})$$

can be substantially lower than the driving frequency, $\Delta\omega$ because the wave may have to advance by several wavelengths before the object can break free.

Once the object is free, it travels from $\xi = \epsilon$ back toward $\xi = 0$ until it once again encounters a region of the traveling wave that can stop it and reverse its motion. The sawtooth oscillator's recovery is not captured by Eq. (A1) and requires a more complete treatment of the sphere's dynamics. Although this model motivates the observed mode of oscillation, therefore, it does not capture such properties as the transition points between operating modes or the complicated dynamical behavior near transitions.

[1] S. Inoue, S. Mogami, T. Ichiyama, A. Noda, Y. Makino and H. Shinoda. "Acoustical boundary hologram for

macroscopic rigid-body levitation." *J. Acoust. Soc. Am.*

- 145**, 328–337 (2019).
- [2] A. Marzo and B. W. Drinkwater. “Holographic acoustic tweezers.” *Proc. Nat. Acad. Sci.* **116**, 84–89 (2019).
- [3] K. Melde, A. G. Mark, T. Qiu and P. Fischer. “Holograms for acoustics.” *Nature* **537**, 518–522 (2016).
- [4] T. Kozuka, K. Yasui, T. Tuziuti, A. Towata and Y. Iida. “Noncontact acoustic manipulation in air.” *Jap. J. Appl. Phys.* **46**, 4948 (2007).
- [5] J. Wu. “Acoustical tweezers.” *J. Acoust. Soc. Am.* **89**, 2140–2143 (1991).
- [6] D. Baresch, J.-L. Thomas and R. Marchiano. “Observation of a single-beam gradient force acoustical trap for elastic particles: acoustical tweezers.” *Phys. Rev. Lett.* **116**, 024301 (2016).
- [7] G. Thalhammer, R. Steiger, M. Meinschad, M. Hill, S. Bernet and M. Ritsch-Marte. “Combined acoustic and optical trapping.” *Biomed. Opt. Express* **2**, 2859–2870 (2011).
- [8] D. G. Grier. “A revolution in optical manipulation.” *Nature* **424**, 810–816 (2003).
- [9] J. Leach, G. Sinclair, P. Jordan, J. Courtial, M. J. Padgett, J. Cooper and Z. J. Laczik. “3D manipulation of particles into crystal structures using holographic optical tweezers.” *Opt. Express* **12**, 220–226 (2004).
- [10] A. Marzo, S. A. Seah, B. W. Drinkwater, D. R. Sahoo, B. Long and S. Subramanian. “Holographic acoustic elements for manipulation of levitated objects.” *Nat. Commun.* **6**, 8661 (2015).
- [11] R. Hirayama, D. M. Plasencia, N. Masuda and S. Subramanian. “A volumetric display for visual, tactile and audio presentation using acoustic trapping.” *Nature* **575**, 320–323 (2019).
- [12] T. Fushimi, B. W. Drinkwater and T. L. Hill. “What is the ultimate capability of acoustophoretic volumetric displays?” *Appl. Phys. Lett.* **116**, 244101 (2020).
- [13] J. C. Crocker and D. G. Grier. “Methods of digital video microscopy for colloidal studies.” *J. Colloid Interface Sci.* **179**, 298–310 (1996).
- [14] D. Allan, C. van der Wel, N. Keim, T. A. Caswell, D. Wieker, R. Verweij, C. Reid, Thierry, L. Grueter, K. Ramos, apiszcz, zoeith, R. W. Perry, F. Boulogne, P. Sinha, pfigliozzi, N. Bruot, L. Uieda, J. Katins, H. Mary and A. Ahmadi. “soft-matter/trackpy: Trackpy v0.4.2.” (2019).
- [15] F. Zheng, Y. Li, H.-S. Hsu, C. Liu, C. Tat Chiu, C. Lee, H. Ham Kim and K. K. Shung. “Acoustic trapping with a high frequency linear phased array.” *Appl. Phys. Lett.* **101**, 214104 (2012).
- [16] Y. Ochiai, T. Hoshi and J. Rekimoto. “Three-dimensional mid-air acoustic manipulation by ultrasonic phased arrays.” *PloS One* **9**, e97590 (2014).
- [17] P. L. Marston. “Axial radiation force of a Bessel beam on a sphere and direction reversal of the force.” *J. Acoust. Soc. Am.* **120**, 3518–3524 (2006).
- [18] T. Čizmar, V. Garcés-Chávez, K. Dholakia and P. Zemánek. “Optical conveyor belt for delivery of sub-micron objects.” *Appl. Phys. Lett.* **86**, 174101 (2005).
- [19] D. B. Ruffner and D. G. Grier. “Optical conveyors: a class of active tractor beams.” *Phys. Rev. Lett.* **109**, 163903 (2012).
- [20] M. A. Abdelaziz and D. G. Grier. “Acoustokinetics: Crafting force landscapes from sound waves.” *Phys. Rev. Res.* **2**, 013172 (2020).
- [21] M. X. Lim, A. Souslov, V. Vitelli and H. M. Jaeger. “Cluster formation by acoustic forces and active fluctuations in levitated granular matter.” *Nature Phys.* **15**, 460–464 (2019).
- [22] L. P. Gor’kov. “On the forces acting on a small particle in an acoustical field in an ideal fluid.” *Sov. Phys. Dokl.* **6**, 773–775 (1962).
- [23] H. Bruus. “Acoustofluidics 7: The acoustic radiation force on small particles.” *Lab Chip* **12**, 1014–1021 (2012).